

Towards Universal Sparse Gaussian Process Potentials: Application to Lithium Diffusivity in Superionic Conducting Solid Electrolytes

Amir Hajibabaei, Chang Woo Myung, and Kwang S. Kim*

*Center for Superfunctional Materials, Department of Chemistry and Department of Physics,
Ulsan National Institute of Science and Technology, Ulsan 44919, Korea*

(Dated: September 29, 2020)

For machine learning of interatomic potentials the sparse Gaussian process regression formalism is introduced with a data-efficient adaptive sampling algorithm. This is applied for dozens of solid electrolytes. As a showcase, experimental melting and glass-crystallization temperatures are reproduced for $\text{Li}_7\text{P}_3\text{S}_{11}$ and an uncharted infelicitous phase is revealed with much lower Li diffusivity which should be circumvented. By hierarchical combinations of the expert models universal potentials are generated, which pave the way for modeling large-scale complexity by a combinatorial approach.

A solid with ionic conductivity similar to liquid electrolytes has far reaching implications for the energy storage industry. Recently, first-principles (FP) calculations have been applied extensively for theoretical studies of ionic diffusion in solid electrolytes [1]. But due to the huge computational resources required for the electronic structure calculations these simulations are often applied only to small systems (~ 100 atoms) and short intervals of time (~ 100 ps). Moreover, due to the Arrhenius-type temperature dependence of the diffusion events in solids, they occur too slowly at room temperature to be sampled with statistical certainty using ab initio molecular dynamics (AIMD) [2]. Therefore often simulations are carried out at elevated temperatures and ionic diffusivity at room temperature is approximated by extrapolation. However, this is not possible in the cases where the system of interest is unstable at higher temperatures.

As an alternative to FP calculations, it has been demonstrated that machine learning (ML) methods can be applied for accurate representations of the potential energy surface (PES). Most notably, neural-network representations [3], Gaussian approximation potentials [4], gradient-domain [5] and symmetrized gradient-domain ML [6], deep potential [7], compressed sensing [8], and deep neural-network for molecular wavefunctions [9] are among various ML techniques which have been implemented. Using these techniques, the PES is learned from the data (potential energy and forces) obtained from limited FP calculations. In particular, the kernel methods pioneered by Bartók et al. [4] can be viewed as smooth interpolations of the energies in the data. For generation of the relevant data, on-the-fly learning [10–12], a query-by-committee active-learning [13], and global exploration of PES [14] have been reported.

Neural-networks scale linearly with the size of data n but they contain a huge number of optimizable parameters and require big data to avoid over-fitting. On the other hand, the kernel methods where a covariance matrix is constructed and inverted, are (almost) non-

parametric but scale as n^2 for construction and n^3 for inversion of the covariance matrix. Considering that a single FP calculation for a system with N atoms yields $3N + 1$ data components, the size of covariance matrix becomes huge even with a small number of training data. Because of this unfavorable scaling, a critical issue is balancing of the global exploration versus local exploitation in sampling the data. For instance, in some on-the-fly learning algorithms the ML model is continuously updated during MD which guaranties the sufficient accuracy but instead undermines its transferability. Here we explore low-rank approximations of the covariance matrix for improving the scalability and an adaptive sampling algorithm for optimal generation of the training data and global exploration. In addition we show that local expert models can be merged to yield a global, transferable, scalable, and accurate universal potential.

Let $\mathbf{x} = \{\rho_j\}_{j=1}^N$ denote a snapshot of a system with N atoms, where ρ_j is the local chemical environment (LCE) of atom j which depends only on the species and relative coordinates of the atoms in the neighborhood of j within a cutoff radius r_c . The data for this snapshot consists of the potential energy E and forces $\{\vec{F}_j\}_{j=1}^N$ obtained by FP calculations. A similarity kernel function $k(\rho, \rho') = \beta^2 \hat{k}(\rho, \rho') \leq \beta^2$ is defined such that $\hat{k}(\rho, \rho) = \hat{k}(\rho', \rho') = 1$. For abstraction, we make a convention that the kernel can also be used for two sets of LCEs and result in a scalar or a matrix. For two sets $A = \{a_j\}$ and $B = \{b_j\}$, we define

$$\text{i } k(A, B) = \sum_{i,j} k(a_i, b_j)$$

$$\text{ii } [k(A, \check{B})]_j = \sum_i k(a_i, b_j)$$

$$\text{iii } [k(\check{A}, \check{B})]_{ij} = k(a_i, b_j)$$

where $k(A, B)$, $k(A, \check{B})$, and $k(\check{A}, \check{B})$ are respectively a scalar, a (column) vector, and a matrix. The above formulas are applied recursively.

Let $\mathbf{X} = \{\mathbf{x}_j\}_{j=1}^n$ denote a set of snapshots and $\mathbf{Y} = \{E_j\}_{j=1}^n$ be their potential energies. A Gaussian process regression (GPR) based on this data, has the following

* kimks@unist.ac.kr

predictive energy E and variance Σ for a test snapshot \mathbf{x}

$$E(\mathbf{x}) = k(\mathbf{x}, \check{\mathbf{X}}) \left(k(\check{\mathbf{X}}, \check{\mathbf{X}}) + \sigma^2 \mathbb{I} \right)^{-1} Y \quad (1)$$

$$\Sigma(\mathbf{x}) = k(\mathbf{x}, \mathbf{x}) - k(\mathbf{x}, \check{\mathbf{X}}) \left(k(\check{\mathbf{X}}, \check{\mathbf{X}}) + \sigma^2 \mathbb{I} \right)^{-1} k(\check{\mathbf{X}}, \mathbf{x}) \quad (2)$$

where σ is a hyper-parameter that conceptually models the noise in the data but even in a noiseless setup a finite value is needed for enforcing the positive-definite requirement of the covariance matrix.

Let $\mathbf{z} = \{\chi_j\}_{j=1}^m$ denote a reduced set of LCEs that is sufficient statistics for \mathbf{X} which may be obtained by random sampling or more sophisticated greedy selection algorithms. The key for a sparse Gaussian process (SGPR) model is low-rank approximation of the full Gram matrix

$$k(\check{\mathbf{X}}, \check{\mathbf{X}}) \approx k(\check{\mathbf{X}}, \check{\mathbf{z}}) k(\check{\mathbf{z}}, \check{\mathbf{z}})^{-1} k(\check{\mathbf{z}}, \check{\mathbf{X}}) = Q^T Q \quad (3)$$

where $k(\check{\mathbf{z}}, \check{\mathbf{z}}) = LL^T$, L is the Cholesky factor, and $Q = L^{-1} k(\check{\mathbf{z}}, \check{\mathbf{X}})$. The inversion problem $(Q^T Q + \sigma^2 \mathbb{I})^{-1}$ is trivial using the matrix inversion lemma. This approximation is achieved by redefining the kernel as

$$\tilde{k}(\rho, \rho') = k(\rho, \check{\mathbf{z}}) k(\check{\mathbf{z}}, \check{\mathbf{z}})^{-1} k(\check{\mathbf{z}}, \rho') \quad (4)$$

and $k \rightarrow \tilde{k}$ substitution of every term including the kernel in Eq. 1. Thus similarity of two LCEs is indirectly calculated using the inter-mediating set \mathbf{z} . This results in a predictive energy given by

$$E(\mathbf{x}) = k(\mathbf{x}, \check{\mathbf{z}}) \mu \quad (5)$$

where, if $U = k(\check{\mathbf{z}}, \check{\mathbf{X}})$, μ is a column vector given by

$$\mu = \left(k(\check{\mathbf{z}}, \check{\mathbf{z}}) + \sigma^{-2} U U^T \right)^{-1} U Y / \sigma^2. \quad (6)$$

It is worth noting that if $k(\check{\mathbf{z}}, \check{\mathbf{z}})$ in the above expression is replaced by $\gamma^{-2} \mathbb{I}$, this formalism will be reduced to the Bayesian linear regression [12] method. Also note that if we substitute $\mu = k(\check{\mathbf{z}}, \check{\mathbf{z}})^{-1} w$ in Eq. 5 it looks like a regression based on (\mathbf{z}, w) (on behalf of \mathbf{X}, Y). Therefore this approximation is also called projected process (PP). SGPR and PP are distinguished only in defining the loss function for optimizing the hyper-parameters and selection of \mathbf{z} . In SGPR the variational lower-bound of the true log marginal likelihood introduced by Titsias [15] should be maximized. For inclusion of the forces data in regression, they can be appended to Y if derivatives of the kernel with respect to atomic positions are appended to U . In the following we will refer to \mathbf{z} as the inducing set of LCEs. A useful quantity that indicates the covariance loss due to sparsification is

$$s(\rho) = k(\rho, \rho) - \tilde{k}(\rho, \rho) \quad (7)$$

which is referred to as the spilling factor [16] but it can also be viewed as the predictive variance of a GPR based on (\mathbf{z}, w) . After projection, only \mathbf{z} and μ are needed for

making predictions, reducing the computational cost to $\mathcal{O}(m)$ instead of $\mathcal{O}(nN)$. This improvement is potentially several orders of magnitude if we also take the forces data into account.

For a similarity kernel between LCEs, a variation of the smooth overlap of atomic positions (SOAP) [17] is developed which takes advantage of series expansion of Bessel-i functions, [18] instead of expansion using a set of radial basis functions (see Supplemental Material (SM) [19]). A package for machine learning of the potential energy surface has been deposited to the github repository [20]. Extension to multi-species environments is straightforward [21].

For adaptive sampling of the data \mathbf{X} and inducing LCEs \mathbf{z} , the model is built on-the-fly with MD where the system evolves with the SGPR potential, and FP calculations are carried out actively to correct the model based on the following criterion. The data and unique LCEs in the first step are automatically included in \mathbf{X} and \mathbf{z} . In the following steps, we try to insert on-the-fly LCEs to \mathbf{z} . Let $\chi_j \in \mathbf{x}(t)$ be the LCE of atom j at time t . Also let $E^{\mathbf{X}, \mathbf{z}}$ be the predicted energy of a model built with \mathbf{X}, \mathbf{z} . χ_j is added to \mathbf{z} only if $|E^{\mathbf{X}, \mathbf{z} + \chi_j}(\chi_j) - E^{\mathbf{X}, \mathbf{z}}(\chi_j)| > \epsilon$ which is the change in the predicted energy for χ_j resulting from its inclusion in \mathbf{z} and ϵ is a predetermined threshold. Since it is too costly to try out all LCEs in $\mathbf{x}(t)$, in the spirit of importance sampling, we try insertion of LCEs based on their spilling factor (Eq. 7) in a descending order and terminate at the first unsuccessful insertion trial. If at least one LCE is added to \mathbf{z} , it means that the system has potentially crossed into an unfamiliar region. At this stage, in one algorithm (FAST), we calculated the exact FP energy and forces for $\mathbf{x}(t)$ and included it in \mathbf{X} (and corresponding energy and forces in Y) if $|E^{\mathbf{X} + \mathbf{x}, \mathbf{z}}(\mathbf{x}) - E^{\mathbf{X}, \mathbf{z}}(\mathbf{x})| > \epsilon$ or $\max_{k, \alpha} |F_{k, \alpha}^{\mathbf{X} + \mathbf{x}, \mathbf{z}}(\mathbf{x}) - F_{k, \alpha}^{\mathbf{X}, \mathbf{z}}(\mathbf{x})| > \epsilon$, similar to the criterion that was applied for extension of \mathbf{z} . Thus, sometimes the exact FP data were regarded as redundant and were rejected by the model. This was devised to keep the number of sampled data (\propto the computation cost in future steps) as small as possible. In another algorithm (ULTRAFast), in order to preempt unwanted FP calculations, predictions of the model were used as fake FP data and if the insertion was accepted they were corrected by exact calculations. This algorithm is similar to leave-one-out cross-validation method for active learning [22]. For promoting global exploration we only sample at the extrema of the on-the-fly potential energy. Special care must be taken for stabilizing the model in early steps. The predictive Bayesian variance could have been used as the criterion for the adaptive sampling, but it was not chosen because low-rank approximation results in over-confident variances or cannot guarantee the positive semidefinite requirement. The selected criterion is more detailed than variance because it also takes advantage of the Y values (i.e the full manifold). Therefore hereafter we will refer to it as the geometric criterion.

The Vienna Ab initio Simulation package (VASP) [23]

which implements the projector augmented-wave [24] approach to DFT with PBE GGA functionals [25] is used for all FP calculations. Calculations are non-spin-polarized and kinetic energy cutoff of 500 eV is applied. We have developed the python package `AutoForce` for generating SGPR models and on-the-fly learning of the PES. [20] This package is coupled with the atomic simulation environment (ASE) [26] and from there it can be coupled to various FP software including VASP.

As the first example, a SGPR model is generated by training in Li_3PS_4 (α and β phases) and $\text{Li}_7\text{P}_3\text{S}_{11}$ crystals. With the algorithm FAST, during total of $\mathcal{O}(10^5)$ MD steps, only 456 FP calculations are performed from which only 111 are sampled and 705 LCEs are sampled as the inducing set. The root mean squared error (RMSE) of the model on the forces of these 456 snapshots is $0.13 \text{ eV } \text{\AA}^{-1}$. The generated model is used for various MLMD (distinct from on-the-fly MD) simulations without further training. To verify the model with data independent from training, we performed lengthy MLMD simulations for $\text{Li}_7\text{P}_3\text{S}_{11}$ at several temperatures in the range 300 to 700 K and 10^3 snapshots are randomly selected from trajectories. For this testing set, the RMSE is $0.14 \text{ eV } \text{\AA}^{-1}$ which is very close to the RMSE of the model on the training data. Therefore sampling algorithm for the purpose of global exploration has been very effective. Note that the magnitude of forces and their errors become larger as temperature increases. In Ref [12] it was shown that from 100 to 400 K the error of their on-the-fly MLMD increased from 0.05 to $0.08 \text{ eV } \text{\AA}^{-1}$ in one case and from 0.09 to $0.12 \text{ eV } \text{\AA}^{-1}$ in another. Since $0.14 \text{ eV } \text{\AA}^{-1}$ is the global error of the SGPR model (not the on-the-fly error), testing MD simulation are at higher temperatures, and the model is built with only ~ 100 snapshots, the SGPR formalism is an important improvement. Training and testing are discussed in more details in SM [19].

The generated SGPR model is used for large scale MLMD simulations of $\text{Li}_7\text{P}_3\text{S}_{11}$ ($4 \times 2 \times 2$ super-cell, 672 atoms) in isothermal-isobaric (NPT) ensemble at several temperatures in the range 300 to 1200 K and external pressure of 10^5 Pa . For this size, our implementation of MLMD is $\mathcal{O}(10^4)$ faster than AIMD. The mean squared displacement (MSD) of atoms, defined by

$$\text{MSD}(t) = \frac{1}{N} \sum_{i=1}^N |\Delta \vec{r}_i(t)|^2 \quad (8)$$

where N is the number of mobile ions and $\Delta \vec{r}_i(t) = \vec{r}_i(t) - \vec{r}_i(0)$, is shown in SM. A phase transition is detected by MLMD (at $T \geq 450$) which occurs by rotations of the P_2S_7 double-tetrahedra into a new orientational order. In the following, the initial and the new structures are referred to as α and β phases. Specifically in the range 450 to 600 K the system remains a few hundred ps in the α -phase before transition to the β -phase which allows us to estimate the Li diffusivity in both phases. In agreement with experimental reports [27, 28], at 900 K,

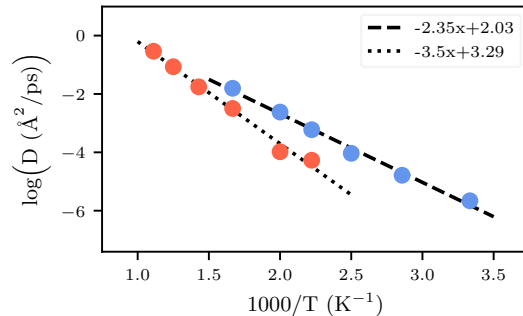


FIG. 1. Li diffusivity in α (blue) and β (red) phases of $\text{Li}_7\text{P}_3\text{S}_{11}$.

the P and S atoms also start to diffuse, which indicates melting or its decomposition to more stable components. The ground state energies of α and β phases (relaxed and calculated with DFT) are -4.413 and -4.416 eV per atom respectively (see SM for visualizations). In addition to being almost iso-energetic, the energy barrier is not large because rotations of P_2S_7 occurs layer-by-layer during MLMD.

The diffusion coefficient (diffusivity) is defined as

$$D = \lim_{t \rightarrow \infty} \frac{1}{2dt} \langle \text{MSD}(t) \rangle \quad (9)$$

where $d = 3$ is dimensions and $\langle \rangle$ indicates the ensemble average. The calculated diffusivities are shown in Fig. 1. With the assumption of an Arrhenius temperature dependence for diffusivity

$$D = D_0 e^{-E_a/k_B T}, \quad (10)$$

we calculate the activation energies E_a of 0.20 eV and 0.30 eV in α and β phases, respectively. The Nernst-Einstein relationship for conductivity σ is given by

$$\sigma = \frac{Nq^2}{Vk_B T} D \quad (11)$$

where N is number of Li atoms, V is volume, q is ions electric charge, and T is temperature. The ionic conductivity in α phase at 300 K becomes $3.5 \times 10^{-2} \text{ S cm}^{-1}$ from direct simulation at this temperature which is in reasonable agreement with previous reports of 5.7×10^{-2} [29] and $4.5 \times 10^{-2} \text{ S cm}^{-1}$ [30]. For β phase, the extrapolated Li diffusivity corresponds to the conductivity of $2.3 \times 10^{-3} \text{ S cm}^{-1}$ at the same temperature which is more than an order of magnitude lower than α phase. The reason for the large drop in diffusivity is discussed in SM.

The glass $\text{Li}_7\text{P}_3\text{S}_{11}$ is created by a melt-quench simulation from 1200 to 300 K. The Li conductivity of $9.3 \times 10^{-3} \text{ S cm}^{-1}$ is then obtained for the glass phase (with MLMD for 3 ns) which is higher than the conductivity in β phase. Equilibration of the glass at higher

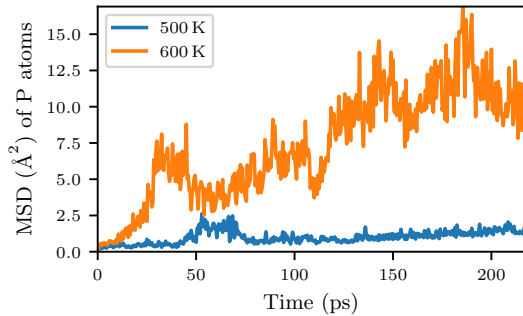


FIG. 2. MSD of P atoms in glass phase $\text{Li}_7\text{P}_3\text{S}_{11}$. Diffusion of these atoms at 600 K indicates crystallization.

temperatures (Fig. 2) shows that P atoms start to diffuse at 600 K which indicates crystallization, in agreement with experiment [27, 28, 31]. In liquid and glass phases RMSE of the SGPR model is $\sim 0.21 \text{ eV } \text{\AA}^{-1}$ (see SM).

Experimentally, $\text{Li}_7\text{P}_3\text{S}_{11}$ is often prepared in glass-ceramic phase by controlled crystallization and heat treatment of the glass phase. Depending on the heat treatment conditions, ionic conductivities of 3.2×10^{-3} and $1.7 \times 10^{-2} \text{ S cm}^{-1}$ are reported [28, 31]. It was shown that the experimental conductivity is correlated with the degree of crystallisation, depending on the heat treatment method [32].

Experimental measurements of the ionic conductivity with techniques such as impedance spectroscopy probe the long-range dynamics of Li which is influenced by the properties such as grain boundaries, degree of amorphism, etc. Wohlmuth et al. [33] probed the short-range diffusivity of Li in glass-ceramic $\text{Li}_7\text{P}_3\text{S}_{11}$ using a range of nuclear magnetic resonance (NMR) methods and concluded that the activation energy of bulk $\text{Li}_7\text{P}_3\text{S}_{11}$ is 0.20 eV in agreement with our simulation. Thus such experimental measurements are crucial for closing the gap between theory and experiment. In SM, we show that grain boundaries modify the activation energy by $E'_a = E_a + (E_g - E_a)/l$ where E_g is the energy barrier at grain boundary and l is the grain size which can often be measured experimentally.

Next, we focus on ternary systems in the `materialsproject` [34] repository which contain Li. In an unsupervised/automated fashion, about 300 structures were chosen with reasonably high band-gap. After brief on-the-fly modeling, 22 crystals showed desired stability and Li diffusivity to be calculable with ~ 100 ps time-scale MLMD simulations. Temperature dependent diffusivity and room temperature ionic conductivity are calculated for this set of materials and listed in Table S1 [19]. Some well known superionic conductors, including $\text{Li}_7\text{P}_3\text{S}_{11}$, appear on top of the list. Here, an “expert” model is created for describing each material. It is intriguing to see how such models perform

TABLE I. RMSE ($\text{eV } \text{\AA}^{-1}$) of expert models and their combinations for Li-P-S and Li-Sb-S systems. e, f or g, h are allotropes. Ex is the expert model for x.

| | | Ea | Eb | Ec | Ed | POE | MOE | FOE |
|---|--|------|------|------|------|------|------|------|
| a | Li_3PS_4 | 0.14 | 0.31 | 0.20 | 0.17 | 0.16 | 0.14 | 0.12 |
| b | Li_7PS_6 | 0.32 | 0.12 | 0.44 | 0.48 | 0.30 | 0.13 | 0.10 |
| c | $\text{Li}_{48}\text{P}_{16}\text{S}_{61}$ | 0.71 | 0.58 | 0.17 | 0.50 | 0.44 | 0.18 | 0.14 |
| d | $\text{Li}_7\text{P}_3\text{S}_{11}$ | 0.53 | 0.58 | 0.33 | 0.18 | 0.32 | 0.18 | 0.15 |

| | | Ee | Ef | Eg | Eh | Ei | POE | MOE | FOE |
|---|---------------------------|------|------|------|------|------|------|------|------|
| e | Li_5SbS_4 | 0.16 | 0.23 | 0.23 | 0.24 | 0.73 | 0.25 | 0.16 | 0.13 |
| f | Li_5SbS_4 | 0.22 | 0.17 | 0.23 | 0.21 | 0.54 | 0.21 | 0.16 | 0.13 |
| g | Li_3SbS_3 | 0.23 | 0.25 | 0.18 | 0.21 | 0.56 | 0.22 | 0.18 | 0.15 |
| h | Li_3SbS_3 | 0.24 | 0.20 | 0.19 | 0.16 | 0.51 | 0.17 | 0.16 | 0.13 |
| i | Li_3SbS_4 | 0.68 | 0.77 | 0.61 | 0.60 | 0.14 | 0.52 | 0.20 | 0.15 |

on other similar materials. For instance 4 materials out of 22 had the same set of elements (Li-P-S). As shown in Table I, while the RMSE of expert models in their domains of expertise is good (0.1 to $0.2 \text{ eV } \text{\AA}^{-1}$), they perform poorly on other materials. By remembering that a SGPR model is fully determined by its data and inducing LCEs, we combined these models with three methods

- product of experts (POE): average of all of the expert models is calculated for making predictions.
- merging of experts (MOE): the data and inducing LCEs of all of the expert models are combined by importance sampling (with the geometric criterion) to give a single compressed model for all materials.
- fusion of experts (FOE): the covariance between data and inducing LCEs of all expert models are fully utilized.

The RMSE of these combined models is shown in Table I. POE globally performs better than the expert models but it lacks the desired precision because no covariance between the experts is assumed. MOE is as good as the expert models even though its size (102 data/573 inducing LCEs) is much smaller than the combined size of the experts (181/1418). FOE has the same size as the combined size of the experts but almost in all of the cases is better than the expert models. Because of much better scalability of MOE, it is preferred for combining a large set of expert models. Similar combinations are shown for Li-Sb-S system in Table I. The MOEs for P and Sb systems can readily be fused to describe all materials in both systems with a single universal potential, but to gain the best scalability a chemical similarity kernel for P and Sb can be defined and optimized. By exploiting their chemical similarity the mutual information can be merged to give the best sparse representation of the PES. The result model can be used for mixed P/Sb systems with no further training as long as P and Sb atoms remain far enough ($\gtrsim 5 \text{ \AA}$).

In conclusion, we used the SGPR formalism for generating accurate, stable, and scalable potentials which, in the cases of $\text{Li}_7\text{P}_3\text{S}_{11}$, described the short-ranged Li diffusivity and melting/crystallization (from glass phase) temperatures, consistent with experiment. An uncharacterized infelicitous crystal structure is found for this material which is nearly iso-energetic to the known crystal structure but has a much lower Li diffusivity. This phase should be avoided for better Li conductivity. Dozens

of other ternary solid electrolytes are also modeled (see [19]). We showed that local expert models can be merged for generating global/universal models. This is a promising strategy for combining ML potentials trained for different materials for describing more complex systems because chemical complexity at larger scales often arises from combinations of a finite set of local patterns.

This work was supported by KISTI (KSC-2018-CHA-0057, KSC-2019-CRE-0253).

-
- [1] Z. Deng, Y. Mo, and S. P. Ong, Computational studies of solid-state alkali conduction in rechargeable alkali-ion batteries (2016).
- [2] X. He, Y. Zhu, A. Epstein, and Y. Mo, Statistical variances of diffusional properties from ab initio molecular dynamics simulations, *npj Computational Materials* **4**, 18 (2018).
- [3] J. Behler and M. Parrinello, Generalized Neural-Network Representation of High-Dimensional Potential-Energy Surfaces, *Physical Review Letters* **98**, 146401 (2007).
- [4] A. P. Bartók, M. C. Payne, R. Kondor, and G. Csányi, Gaussian Approximation Potentials: The Accuracy of Quantum Mechanics, without the Electrons, *Physical Review Letters* **104**, 136403 (2010).
- [5] S. Chmiela, A. Tkatchenko, H. E. Sauceda, I. Poltavsky, K. T. Schütt, and K.-R. Müller, Machine learning of accurate energy-conserving molecular force fields, *Science Advances* **3**, e1603015 (2017).
- [6] S. Chmiela, H. E. Sauceda, K.-R. Müller, and A. Tkatchenko, Towards exact molecular dynamics simulations with machine-learned force fields, *Nature Communications* **9**, 3887 (2018).
- [7] L. Zhang, J. Han, H. Wang, R. Car, and W. E, Deep Potential Molecular Dynamics: A Scalable Model with the Accuracy of Quantum Mechanics, *Physical Review Letters* **120**, 143001 (2018).
- [8] A. Seko, A. Takahashi, and I. Tanaka, First-principles interatomic potentials for ten elemental metals via compressed sensing, *Physical Review B* **92**, 054113 (2015).
- [9] K. T. Schütt, M. Gastegger, A. Tkatchenko, K. R. Müller, and R. J. Maurer, Unifying machine learning and quantum chemistry – a deep neural network for molecular wavefunctions, *Nature Communications* **10**, 5024 (2019).
- [10] Z. Li, J. R. Kermode, and A. De Vita, Molecular Dynamics with On-the-Fly Machine Learning of Quantum-Mechanical Forces, *Physical Review Letters* **114**, 096405 (2015).
- [11] R. Jinnouchi, F. Karsai, and G. Kresse, On-the-fly machine learning force field generation: Application to melting points, *Physical Review B* **100**, 014105 (2019).
- [12] R. Jinnouchi, J. Lahnsteiner, F. Karsai, G. Kresse, and M. Bokdam, Phase Transitions of Hybrid Perovskites Simulated by Machine-Learning Force Fields Trained on the Fly with Bayesian Inference, *Physical Review Letters* **122**, 225701 (2019).
- [13] N. Artrith and J. Behler, High-dimensional neural network potentials for metal surfaces: A prototype study for copper, *Physical Review B* **85**, 045439 (2012).
- [14] N. Bernstein, G. Csányi, and V. L. Deringer, De novo exploration and self-guided learning of potential-energy surfaces, *npj Computational Materials* **5**, 99 (2019).
- [15] M. Titsias, Variational Learning of Inducing Variables in Sparse Gaussian Processes, in *Proceedings of the Twelfth International Conference on Artificial Intelligence and Statistics*, Proceedings of Machine Learning Research, Vol. 5, edited by D. van Dyk and M. Welling (PMLR, Hilton Clearwater Beach Resort, Clearwater Beach, Florida USA, 2009) pp. 567–574.
- [16] K. Miwa and H. Ohno, Molecular dynamics study on β -phase vanadium monohydride with machine learning potential, *Physical Review B* **94**, 184109 (2016).
- [17] A. P. Bartók, R. Kondor, and G. Csányi, On representing chemical environments, *Physical Review B* **87**, 184115 (2013).
- [18] G. N. G. N. Watson, *A treatise on the theory of Bessel functions* (Cambridge University Press, 1995) p. 804.
- [19] See Supplemental Material at [URL will be inserted by publisher] for descriptor and kernel function, training and testing, visualizations, effect of grain boundaries, and table of ternary solid electrolytes.
- [20] A. Hajibabaei, Python package for sparse Gaussian process regression of ab-initio calculations (2019).
- [21] S. De, A. P. Bartók, G. Csányi, and M. Ceriotti, Comparing molecules and solids across structural and alchemical space, *Physical Chemistry Chemical Physics* **18**, 13754 (2016).
- [22] H. Liu, Y. S. Ong, and J. Cai, A survey of adaptive sampling for global metamodeling in support of simulation-based complex engineering design (2018).
- [23] G. Kresse and J. Furthmüller, Efficient iterative schemes for ab initio total-energy calculations using a plane-wave basis set, *Physical Review B - Condensed Matter and Materials Physics* **54**, 11169 (1996).
- [24] P. E. Blöchl, Projector augmented-wave method, *Physical Review B* **50**, 17953 (1994).
- [25] J. P. Perdew, M. Ernzerhof, and K. Burke, Rationale for mixing exact exchange with density functional approximations, *Journal of Chemical Physics* **105**, 9982 (1996).
- [26] A. Hjorth Larsen, J. Jørgen Mortensen, J. Blomqvist, I. E. Castelli, R. Christensen, M. Dulak, J. Friis, M. N. Groves, B. Hammer, C. Hargus, E. D. Hermes, P. C. Jennings, P. Bjerre Jensen, J. Kermode, J. R. Kitchin, E. Leonhard Kolsbjerg, J. Kubal, K. Kaasbjerg, S. Lysgaard, J. Bergmann Maronsson, T. Maxson, T. Olsen, L. Pastewka, A. Peterson, C. Rostgaard, J. Schiøtz, O. Schütt, M. Strange, K. S. Thygesen, T. Vegge, L. Vilhelmsen, M. Walter, Z. Zeng, and K. W. Jacobsen, The atomic simulation environment - A Python library for working with atoms (2017).
- [27] F. Mizuno, A. Hayashi, K. Tadanaga, and M. Tatsumi

- isago, High lithium ion conducting glass-ceramics in the system $\text{Li}_2\text{SP}_2\text{S}_5$, *Solid State Ionics* **177**, 2721 (2006).
- [28] H. Yamane, M. Shibata, Y. Shimane, T. Junke, Y. Seino, S. Adams, K. Minami, A. Hayashi, and M. Tatsumisago, Crystal structure of a superionic conductor, $\text{Li}_7\text{P}_3\text{S}_{11}$, *Solid State Ionics* **178**, 1163 (2007).
- [29] I. H. Chu, H. Nguyen, S. Hy, Y. C. Lin, Z. Wang, Z. Xu, Z. Deng, Y. S. Meng, and S. P. Ong, Insights into the Performance Limits of the $\text{Li}_7\text{P}_3\text{S}_{11}$ Superionic Conductor: A Combined First-Principles and Experimental Study, *ACS Applied Materials and Interfaces* **8**, 7843 (2016).
- [30] Y. Wang, W. D. Richards, S. H. Bo, L. J. Miara, and G. Ceder, Computational Prediction and Evaluation of Solid-State Sodium Superionic Conductors $\text{Na}_7\text{P}_3\text{X}_{11}$ ($X = \text{O}, \text{S}, \text{Se}$), *Chemistry of Materials* **29**, 7475 (2017).
- [31] Y. Seino, T. Ota, K. Takada, A. Hayashi, and M. Tatsumisago, A sulphide lithium super ion conductor is superior to liquid ion conductors for use in rechargeable batteries, *Energy Environ. Sci.* **7**, 627 (2014).
- [32] Y. Seino, M. Nakagawa, M. Senga, H. Higuchi, K. Takada, and T. Sasaki, Analysis of the structure and degree of crystallisation of $70\text{Li}_2\text{S}-30\text{P}_2\text{S}_5$ glass ceramic, *Journal of Materials Chemistry A* **3**, 2756 (2015).
- [33] D. Wohlmuth, V. Epp, and M. Wilkening, Fast Li Ion Dynamics in the Solid Electrolyte $\text{Li}_7\text{P}_3\text{S}_{11}$ as Probed by ${}^6,7\text{Li}$ NMR Spin-Lattice Relaxation, *ChemPhysChem* **16**, 2582 (2015).
- [34] A. Jain, S. P. Ong, G. Hautier, W. Chen, W. D. Richards, S. Dacek, S. Cholia, D. Gunter, D. Skinner, G. Ceder, and K. A. Persson, Commentary: The materials project: A materials genome approach to accelerating materials innovation (2013).